



OPEN ACCESS

EDITED BY

Patrick Antolin,
Northumbria University, United Kingdom

REVIEWED BY

Meng Jin,
Lockheed Martin Solar and Astrophysics
Laboratory (LMSAL), United States
Daniele Telloni,
National Institute of Astrophysics (INAF),
Italy

*CORRESPONDENCE

David H. Brooks,
✉ dhbrooks.work@gmail.com

SPECIALTY SECTION

This article was submitted to Stellar and
Solar Physics, a section of the journal
Frontiers in Astronomy and Space
Sciences

RECEIVED 23 January 2023

ACCEPTED 15 March 2023

PUBLISHED 29 March 2023

CITATION

Brooks DH, Reep JW, Ugarte-Urra I and
Warren HP (2023), On orbit performance
of the solar flare trigger for the Hinode
EUV imaging spectrometer.
Front. Astron. Space Sci. 10:1149831.
doi: 10.3389/fspas.2023.1149831

COPYRIGHT

© 2023 Brooks, Reep, Ugarte-Urra and
Warren. This is an open-access article
distributed under the terms of the
[Creative Commons Attribution License
\(CC BY\)](#). The use, distribution or
reproduction in other forums is
permitted, provided the original author(s)
and the copyright owner(s) are credited
and that the original publication in this
journal is cited, in accordance with
accepted academic practice. No use,
distribution or reproduction is permitted
which does not comply with these terms.

On orbit performance of the solar flare trigger for the Hinode EUV imaging spectrometer

David H. Brooks^{1*}, Jeffrey W. Reep², Ignacio Ugarte-Urra² and Harry P. Warren²

¹College of Science, George Mason University, 4400 University Drive, Fairfax, VA, United States, ²Space Science Division, Naval Research Laboratory, Washington, DC, United States

We assess the on-orbit performance of the flare event trigger for the Hinode EUV Imaging Spectrometer. Our goal is to understand the time-delay between the occurrence of a flare, as defined by a prompt rise in soft X-ray emission, and the initiation of the response observing study. Wide (266") slit patrol images in the He II 256.32 Å spectral line are used for flare hunting, and a response is triggered when a pre-defined intensity threshold is reached. We use a sample of 13 > M-class flares that successfully triggered a response, and compare the timings with soft X-ray data from GOES, and hard X-ray data from RHESSI and Fermi. Excluding complex events that are difficult to interpret, the mean on orbit response time for our sample is 2 min 10 s, with an uncertainty of 84 s. These results may be useful for planning autonomous operations for future missions, and give some guidance as to how improvements could be made to capture the important impulsive phase of flares.

KEYWORDS

solar flare, solar instrumentation, solar activity, instrument performance, EUV spectroscopy

1 Introduction

A central goal of heliophysics research is to understand the build-up, storage, and release of magnetic energy during solar flares and coronal mass ejections (CMEs). As well as scientific understanding of the phenomena themselves, another eventual goal is to develop the ability to predict their occurrence, and mitigate the effects of CME and energetic particle impact on the terrestrial space environment.

High spatial and temporal resolution extreme ultraviolet (EUV) imaging of almost all flares on the Earth-facing side of the Sun is possible with full-disk EUV instruments such as the Atmospheric Imaging Assembly (AIA, [Lemen et al., 2012](#)) on the Solar Dynamics Observatory (SDO, [Pesnell et al., 2012](#)). For deeper scientific insights, however, spectroscopic diagnostic measurements are highly desirable. The drawback is that current EUV spectrometer fields-of-view (FOV) are limited (typically covering something like ~250" x 500") and the slit rastering times are slow (typical timescales of hours), so such observations are not ideal for capturing dynamic events. Full-disk imaging with slit spectrometers is possible and has occasionally been carried out ([Thompson and Brekke, 2000](#); [Brooks et al., 2015](#); [Bryans et al., 2020](#)), but the scanning times are even slower. Routine full-disk scans by the Hinode EUV Imaging Spectrometer (EIS, [Culhane et al., 2007](#)), for example, take about 40 h to complete. Proposed future missions for full-disk spectroscopy could improve this situation ([Ugarte-Urra et al., 2023](#)), but for the near term, spectroscopic

instruments in development, such as Solar-C EUVST and MUSE (MUlti-slit Solar Explorer, De Pontieu et al., 2020), will be limited to relatively small fields-of-view.

The scientific value of these observations is high. EIS, for example, has a wide range of spectral diagnostics that allow measurements of temperatures, densities, elemental abundances, Doppler and non-thermal velocities, and coronal magnetic field strengths in flares (Doschek et al., 2018; Warren et al., 2018; Landi et al., 2021; To et al., 2021). For reviews of flare observations by EIS see, e.g., Milligan. (2015) and Hinode Review Team et al. (2019). The downside is that the small FOV and slow scanning times make it difficult to capture flares. Together with the difficulty in predicting which active regions are likely to flare, especially when there are multiple possible targets on disk, and restrictions on the quantities of data that can be telemetered to ground, it becomes challenging to maximise the scientific output.

There have been some studies of the success rate of flare observations for instruments such as EIS. Inglis et al. (2021) simulated the performance of a small FOV mission depending on different operational and pointing selection strategies. They found that the most successful strategy for capturing flares was based on response to actual flaring activity in the previous 24 h. Depending on whether the satellite was placed in low Earth orbit, or had continuous solar observing coverage, 35%–62% of M- and X-class flares could be captured with our current forecasting abilities and observing strategies. An important result is that they also found that the success rate was highly dependent on the delay time between acquiring target information and re-pointing the instrument/spacecraft. A quick response is vital.

Watanabe et al. (2012) found that for the first 5 years of the Hinode mission, EIS was able to observe on the order of 15% of flares that reached C-class, as defined by the Geostationary Operational Environmental Satellites (GOES). The percentage is higher (20%) for M- and X-class flares. These figures, however, do not take account of the fact that in periods of high solar activity there can be multiple flaring regions on disk at the same time and, as discussed, EIS cannot observe all of them because of its small FOV. In that sense, the numbers do not necessarily reflect how good the target selection strategy was, since the presence of several flaring ARs can dilute the numbers. The rate has also evolved as a result of improved strategies for flare observing during the mission, but it should be noted that lower telemetry observing studies that can run for a long duration are likely more successful at capturing flares than higher cadence studies with more diagnostics that can only be used for shorter periods.

An alternative to routine observing modes that monitor for flares is to implement an on board autonomous event trigger that responds to flare occurrence. In this way a low cadence flare monitoring program can switch to a higher cadence study when an event is detected. For EIS the data volume for download each day is on the order of ~ 750 Mb. A typical flare response study that is currently used consumes 270 Mb per hour, so it is clear that the trigger can make better use of the available telemetry. Furthermore, a quick response to a flare potentially allows observations of the important impulsive phase (Harra et al., 2009; Jeffrey et al., 2018). Note that the currently available data volume for EIS is about 15%–20% of the original baseline as a result of an issue with the X-band antenna in 2007 (Hinode Review Team et al., 2019). This limitation

was somewhat mitigated by an increase in the number of downlink stations worldwide, and the introduction of more flexible control of data acquisition.

For EIS the pre-flight scientific requirement was to react and initiate a response program within 30 s of flare detection. This requirement is met by the on-board software: the mean time to start the response study from the trigger time in our sample of observations (see below) is 17.2 s. This does not, however, tell us how quickly the instrument responds in practice to the start of the actual flare, information that is important for the development of future missions. Here we investigate the response times for a sample of large flares captured by the EIS flare trigger on orbit and report the results.

2 Method

Hinode/EIS is described in detail by Culhane et al. (2007). The instrument is a normal incidence spectrograph that observes in two wavelength ranges from 171 to 211 Å and 245–291 Å with a spectral resolution of 23 mÅ. A rotating slit assembly allows the use of four different apertures of 1", 2", 40", and 266" widths. EIS has two internal and one external solar event triggers. Internally there is a bright point trigger. This locates an area of maximum (pre-defined) intensity within a narrow slit (1" or 2") raster scan and its functionality is discussed in EIS software note No. 14 by Young (2011)¹. A key point is that the raster scan is completed before the response study begins, so one drawback is that the detection is slow. Hence this trigger is not suitable for determining how quickly EIS responds to the appearance of a bright point. It is also not suitable for observing flares. Externally, EIS can respond to a flare flag raised by Hinode/XRT (X-ray Telescope, Golub et al., 2007). In this case, EIS takes patrol images purely to switch into flare response mode (one image is enough). There is no relationship between the patrol images and the trigger for the flare. These two event triggers are not discussed further here. EIS also has its own internal flare trigger (EFT). In this brief report we focus on the performance of this event trigger.

For flare hunting with the EFT, the 266" wide-slit is used to monitor a typical FOV of 266" × 512". Typically the He II 256.32 Å spectral line is selected for active region monitoring, though experiments with Fe XXIV 192.04 Å have also been undertaken. The advantage of He II is that the upper chromosphere often brightens first (in response to the impact of non-thermal electrons) before post-flare loops begin to be filled with higher temperature emitting plasma (that would trigger in Fe XXIV or soft X-rays). We note that opacity effects that radiatively couple different points within the emitting plasma can affect the emergent intensities of He II 256.32 Å. Whether this has any effect on the speed of production of an observable flare signature is an open question. It could be that another optically thin, or weakly modified optically thick, chromospheric or transition region line would lead to an improved trigger performance.

A detection algorithm is run on each exposure. This compares the He II 256.32 Å intensity distributions in the X- and Y- directions on the detector with several pre-defined criteria. First, the intensities

1 http://solarb.mssl.ucl.ac.uk/SolarB/eis_docs/eis_notes/14_BP_TRIGGER/eis_swnote_14.pdf.

are summed along each row and column in the image. Note that the column intensities correspond to the solar-Y direction. Because the wide-slit is used, however, the spatial and spectral information is convolved in the dispersion direction and the row intensities correspond to positions in solar-X and wavelength. Second, the summed row and column intensity distributions are compared to pre-defined thresholds, and the number of pixels that exceed the thresholds in both directions are recorded. Third, a check is made to determine how many of the excess pixels occur consecutively in each direction. If these numbers exceed another pre-defined threshold then the flare response is triggered. We show an illustration of the functionality of the algorithm in the next section.

All of the thresholds can be adjusted by the EIS Chief Observer, but in practice care has to be taken so experiments were performed to find the best values and these are not routinely changed. For example, in the Y-direction, the EIS slit is long, so the active region contribution to the summed intensity can be relatively small. The threshold in this direction is therefore set relatively low so that the detection criteria are almost always satisfied by a flare. On-orbit testing determined that a value of 350,000 DN successfully triggers. In the X-direction, the threshold is set higher so that only large flares are detected. Again, on-orbit testing determined that a value of 400,000 DN is high enough to exclude events weaker than around M-class. Currently, the same thresholds are used for all EFT runs. The consecutive-pixels lower limit is implemented to avoid triggering on energetic particle hits. Hinode passes through the South Atlantic Anomaly (SAA) and High-Latitude Zone (HLZ) several times per day, but energetic particles tend to light up only a few pixels, or streak across the detector so that they are not clustered consecutively. Although it is difficult to assess the history of the whole mission, we are not aware of any occasions when the flare trigger was activated by SAA passage.

Once the flare occurrence criteria are satisfied, the flare coordinates are determined. This can be done in two ways. The row and column summed intensities are examined to find either the location of the peak intensity in the X- and Y-directions, or the center pixel between the first and last crossing of the threshold (in both directions). The EIS Chief Observer can choose which method is used, but in practice the peak is normally used. EIS then re-points to the flare location using its fine mirror, and runs a pre-defined response study, typically with a greater selection of diagnostic lines, higher cadence, shorter exposures (to avoid saturation), and higher telemetry output.

To compare the EFT detection times with the start of a flare we analyzed soft X-ray (SXR) and hard X-ray (HXR) observations from GOES, the Reuven Ramaty High Energy Solar Spectroscopic Imager (RHESSI, Lin et al., 2002) and the Fermi Gamma-ray Burst Monitor (GBM, Meegan et al., 2009). The GOES data were downloaded using the GOES workbench available in SolarSoftware (SSW, Freeland and Handy, 1998). This software returns high cadence (2 s) data in the 1.0–8.0 Å channel from the GOES satellite operating during the selected time-period. The data are archived at the NOAA (National Oceanic and Atmospheric Administration) Space Weather Prediction Center (SWPC) in Boulder, CO. For RHESSI and Fermi, we used data from the 20–50 keV energy channel. These data were retrieved from using the OSPEX (Objective Spectral Executive) software in SSW (Tolbert and Schwartz, 2020). The Fermi/GBM data were obtained from the NASA host website and the

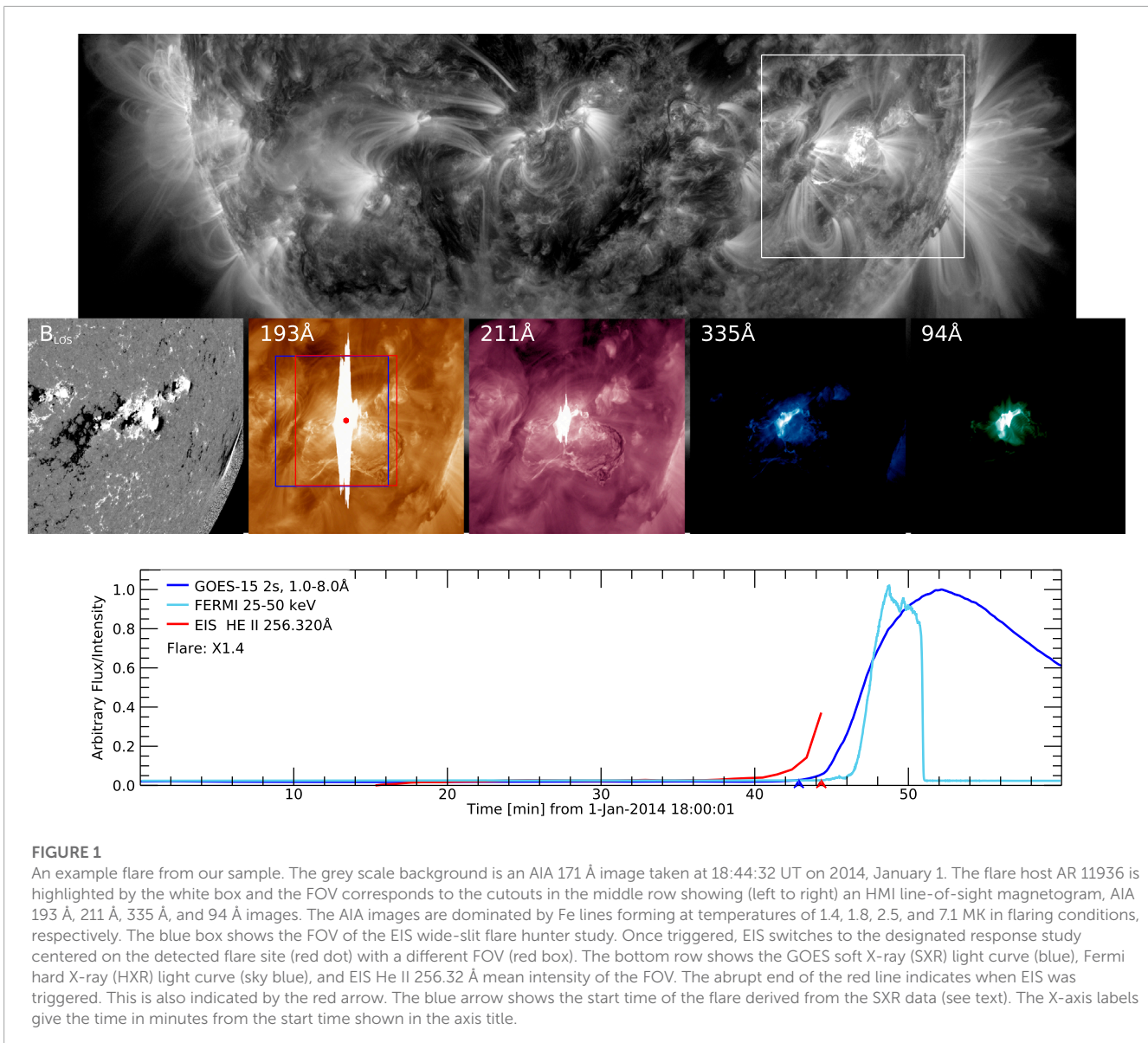
RHESSI data were transferred from the mirror site at the University of California, Berkeley. All the EIS data were processed using the standard (eis_prep) calibration routines available in SSW.

We analyzed a sample of 13 > M-class flares that were successfully detected by the EFT. We used the Hinode Flare Catalog (Watanabe et al., 2012) to find M- and X-class flares that were observed by EIS, and cross-checked which ones were captured by the EIS flare response study. For all these observations the He II 256.32 Å spectral line was used for flare hunting. Examining the response time requires a definition of the flare start time. The cataloged NOAA GOES start times are defined as a steep monotonic increase in the 1.0–8.0 Å flux in a sequence of 4 min, but they use 1–5 min average data and take the first minute as the onset time. For an EFT reaction time measured in seconds, we need a start time defined to a similar time-resolution. We therefore follow their approach and define the start of the flare as the time when the GOES SXR flux increases promptly above the background, but using the high cadence (2 s) data. Furthermore, we adopt a flexible definition of the prompt increase, since our sample of flares is small enough for us to examine their characteristics individually. Specifically, we take a 4 min running mean of the background, and record when the SXR flux increases by 30%. In a few cases we lowered the threshold to 20% or increased it to 50%. This variable threshold is necessary because although most of the flares are large, impulsive events, a few of them occur in the decaying tail of a previous flare so that the background is already high. The EIS trigger times were taken from the time of the exposure that met the trigger criteria. The algorithm, of course, checks after the exposure is made, so there can be some latency that depends on the exposure time. For our sample, the exposure time is 5 s.

3 Results

We show an example of one of the flares in our sample in **Figure 1**. The X1.4 flare occurred in AR 11936 on 2014, January 1. The HMI magnetogram shows that AR 11936 had a magnetically complex $\beta\gamma\delta$ configuration. The GOES SXR flux shows that the flare began at 18:42:52 UT, with a steep rise in the Fermi HXR emission a couple of minutes later. EIS was running its flare hunter study from around 18:10 UT and the He II 256.32 Å intensity began to increase from around 18:42 UT. The lower panel plot gives the impression that EIS triggered earlier than the SXR rise, but of course the intensity has to reach the detection threshold before the instrument responds. The detection is actually at 18:44:19 UT, 87 s after the SXR flare start time.

Figure 2 shows the He II 256.32 Å intensity images in the 6 min leading up to the flare. Note that the first 87 s of the flare are not completely missed. Two patrol images are taken in He II 256.32 Å. Even these images can be used to potentially deconvolve velocity information on the flare onset (Harra et al., 2017). There is a conspicuous pre-flare brightening, however, that is seen even earlier than the GOES flare start time, and therefore might be the ideal trigger. The lower row in the figure illustrates what is happening with the flare detection algorithm during this sequence of images. As discussed in the previous section, the row sum threshold is set to 400,000 DN, and the column sum threshold is set to 350,000 DN, as is the case for most current runs. Neither intensity distribution



exceeds the threshold until just before the GOES start time (5th frame at 18:42:25 UT). At this time more than 13 consecutive pixels exceed the threshold in the Y-direction. That is, the lower column threshold has triggered. The row sum threshold, however, is not exceeded until 18:44:19 UT, although it is close in the previous frame. By this time, all the threshold criteria are met, including the 7 consecutive-pixel limit, and the flare triggers. We can conclude that the trigger could have detected the flare one frame earlier if a lower row sum threshold were used. The pre-flare brightening looks detectable even earlier in the column sum intensity distribution if a lower intensity threshold were used, but it perhaps looks difficult to detect at all in the row summed intensities. The success of the detection criteria are of course flare dependent. Note that using the peak intensities locates the flare at a pixel coordinate of [112,147].

Figure 3 shows the results for the remaining 12 flares in our sample. We used the HXR data from RHESSI when available. Sometimes the data were compromised by changes in attenuator state during the flare, or were affected by eclipses and other issues.

In these cases we used the Fermi/GBM data. On occasion Fermi data were also not available. In these cases we used the derivative of the GOES SXR flux as a proxy for the HXR emission, based on the Neupert effect (Neupert, 1968). **Table 1** gives some relevant details of our flare sample such as the GOES-class, defined GOES start time, measured delay until the triggered response, and flare location.

Figure 4 summarizes the time-delay between the GOES SXR start time and the EIS triggered response for each flare. Generally, the EFT appears to be quite well tuned to the start of the flare and responds promptly, within ~2 min. There is one outlier case where the time-delay is long (947 s). On closer inspection, however, there are extenuating circumstances. This M2.1 flare occurred on 2011, November 6, and is shown in the top left panel of **Figure 3**. In this example, the flare has a double peak at -06:24 UT and -06:36 UT. Our algorithm defines the start time as an increase above the background at 06:16 UT, before the first (lower GOES-class) burst. In fact the EFT hunter study did not start until 06:17 UT, after the flare had begun. Of course a flare was occurring so EIS should trigger, but

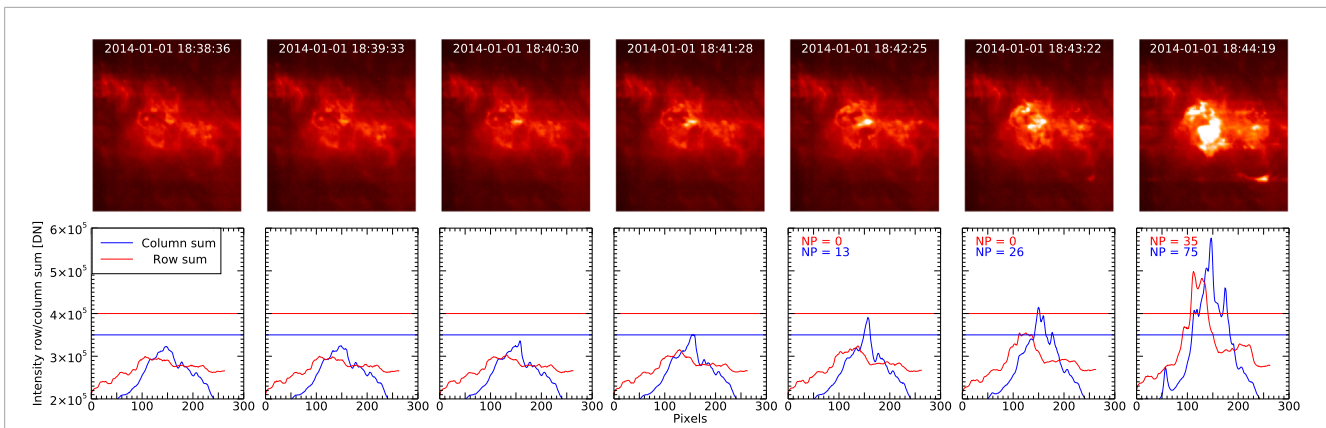


FIGURE 2
 Illustration of the functionality of the EFT detection algorithm for the flare shown in [Figure 1](#). The top row shows EIS He II 256.32 Å wide-slit hunter images in the 6 min leading up to the flare detection. The bottom row shows how the algorithm is evaluating the intensity distributions in the images. The solid red/blue lines show the intensities summed along the rows/columns. The horizontal blue/red lines show the detection thresholds. The number of points above the detection threshold are given in the legend. The X-axis labels show spatial pixels in the solar-X direction.

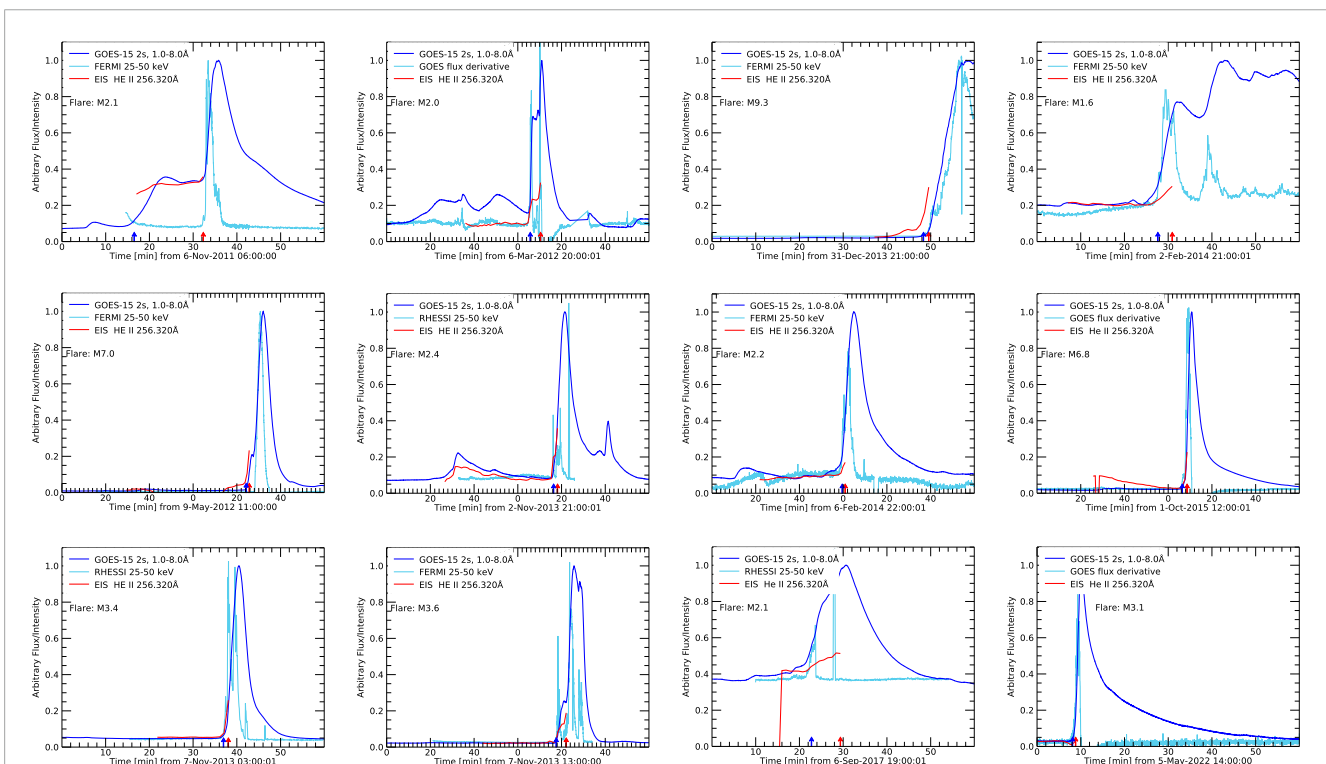


FIGURE 3
 Same as the bottom row of [Figure 1](#) for the other flares in our sample. The X-axis labels give the time in minutes from the start time shown in the axis title. The change to 0 in some of the plots indicates 1 h.

the fact that there is a pedestal and/or decrease in SXR flux before the M2.1 peak apparently fools the EFT into not detecting the conditions to trigger. When encountering the second peak, however, the EFT apparently does trigger fast (62 s early).

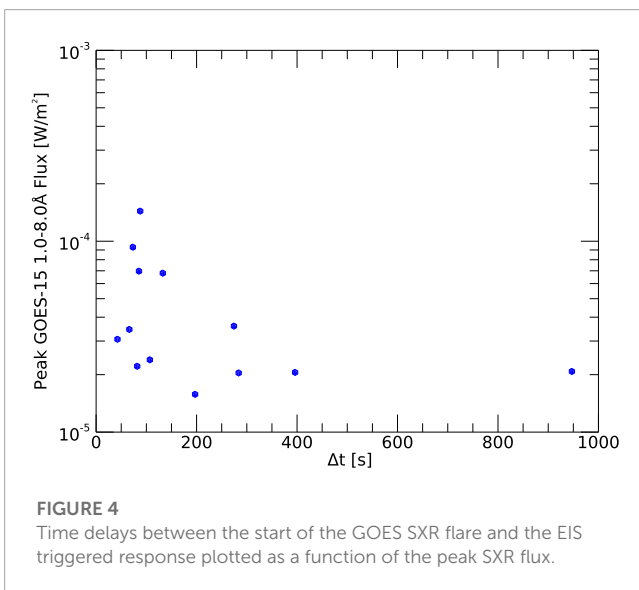
There is another similar case on 2017, September 6 (third panel bottom row in [Figure 3](#)). For this flare, the time-delay is 396 s, which is relatively long. This flare, however, is triggering in the tail of

decreasing SXR flux from an X9.3 event that occurred 7 h before at ~12 UT. This potentially affected the assessment of the background level before the flare.

Excluding these two cases the mean response time for the sample is 130 s. The uncertainty (standard deviation of the time delays for the sample) is 84 s. In the best case, the highly impulsive M3.1 flare on 2022, May 5, the EFT responds in 42 s.

TABLE 1 GOES-15 start time and class are derived from the 2 s high cadence 1.0–8.0 Å data. Δt is the time delay between the GOES-15 start time and the EFT response. Locations are taken from the Hinode Flare Catalog.

GOES-15 SXR Start Time [UT]	GOES-15 Class	EIS Δt [s]	Location
6-Nov-2011 06:16:31	M2.1	947.2	N21E33
6-Mar-2012 21:05:40	M2.0	283.8	N16E30
9-May-2012 12:24:14	M7.0	85.4	N13E31
2-Nov-2013 22:16:21	M2.4	107.0	S12W11
7-Nov-2013 03:36:57	M3.4	66.2	S14E28
7-Nov-2013 14:17:33	M3.6	274.4	S13E23
31-Dec-2013 21:48:20	M9.3	73.2	S16W35
1-Jan-2014 18:42:52	X1.4	87.8	S14W47
2-Feb-2014 21:27:38	M1.6	197.1	S10E01
6-Feb-2014 22:59:33	M2.2	81.8	S15W48
1-Oct-2015 13:06:25	M6.8	132.8	S23W64
6-Sep-2017 19:22:45	M2.1	396.1	S08W38
5-May-2022 14:08:07	M3.1	42.5	S29E64



4 Discussion

We assessed the on-orbit performance of the EIS internal flare trigger from a sample of 13 > M-class flares that were successfully captured. Excluding two events that were complex to interpret, the mean delay-time between the GOES SXR onset time and the EFT response was 2 min 10 s. We conclude that the EFT, based on intensity thresholding in the He II 256.32 Å spectral line, is able to react fairly early in the flare evolution.

Of course there may be scientific studies focused even earlier in the flare impulsive phase, so it makes sense to consider potential

improvements, not just for EIS, but for future missions such as MUSE and Solar-C EUVST. The ~2 min delay suggests that for EIS the detection thresholds could potentially be reduced, and we showed one example where the flare could have been triggered 1–2 min earlier.

When comparing with the HXR data we initially used the GOES SXR derivative as a proxy. Dennis and Zarro. (1993) showed that, following the Neupert effect, peaks in the GOES SXR derivative plot corresponded to peaks in the HXR data to within ± 20 s in 88% of the flares they analyzed. Our analysis found that the EFT time is closer to the onset of the increase in HXR, suggesting that this might even be a better trigger criteria. This initial conclusion does not look as convincing when we look at the actual HXR data from RHESSI and Fermi in Figure 3. In several cases the HXR onset follows the SXR rise. This could reflect the specific characteristics of the flares in our sample. Dennis and Zarro. (1993) did find that the correlation between the SXR time derivative and HXR time profile decreased to 50% for larger (> X1), gradual events in their study.

Conversely, it would not be practical to try to implement an on-board algorithm that triggers off of a spacecraft to spacecraft transmission, so an internal running difference of the derivative of a time-series of intensities from a high temperature line already included in the design wavelength selection (such as Fe XXIV 192.04 Å) could be worth investigating for future missions if chromospheric or transition region coverage is limited.

Data availability statement

Publicly available datasets were analyzed in this study. This data can be found here: <http://solarb.mssl.ucl.ac.uk/SolarB/SearchArchive.jsp>.

Author contributions

Discussions between the authors initiated the study. DB performed the analysis and wrote the paper. JR processed the RHESSI and Fermi data. All authors discussed the results and commented on the manuscript.

Funding

This work was funded by the NASA Hinode program.

Acknowledgments

Hinode is a Japanese mission developed and launched by ISAS/JAXA, with NAOJ as domestic partner and NASA and STFC (UK) as international partners. It is operated by these agencies in co-operation with ESA and NSC (Norway). The AIA images

are courtesy of NASA/SDO and the AIA, EVE, and HMI science teams.

Conflict of interest

The authors declare that the research was conducted in the absence of any commercial or financial relationships that could be construed as a potential conflict of interest.

References

- Brooks, D. H., Ugarte-Urra, I., and Warren, H. P. (2015). Full-Sun observations for identifying the source of the slow solar wind. *Nat. Commun.* 6, 5947. doi:10.1038/ncomms6947
- Bryans, P., McIntosh, S. W., Brooks, D. H., and De Pontieu, B. (2020). Investigating the chromospheric footpoints of the solar wind. *ApJL* 905, L33. doi:10.3847/2041-8213/abce69
- Culhane, J. L., Harra, L. K., James, A. M., Al-Janabi, K., Bradley, L. J., Chaudry, R. A., et al. (2007). The euV imaging spectrometer for hinode. *Sol. Phys.* 243, 19–61. doi:10.1007/s01007-007-0293-1
- De Pontieu, B., Martínez-Sykora, J., Testa, P., Winebarger, A. R., Daw, A., Hansteen, V., et al. (2020). The multi-slit approach to coronal spectroscopy with the multi-slit solar explorer (MUSE). *ApJ* 888, 3. doi:10.3847/1538-4357/ab5b03
- Dennis, B. R., and Zarro, D. M. (1993). The Neupert effect - what can it tell us about the impulsive and gradual phases of solar flares. *Sol. Phys.* 146, 177–190. doi:10.1007/BF00662178
- Doschek, G. A., Warren, H. P., Harra, L. K., Culhane, J. L., Watanabe, T., and Hara, H. (2018). Photospheric and coronal abundances in an X8.3 class limb flare. *ApJ* 853, 178. doi:10.3847/1538-4357/aaa4f5
- Freeland, S. L., and Handy, B. N. (1998). Data analysis with the solarsoft system. *Sol. Phys.* 182, 497–500. doi:10.1023/A:1005038224881
- Golub, L., DeLuca, E., Austin, G., Bookbinder, J., Caldwell, D., Cheimets, P., et al. (2007). The x-ray telescope (xrt) for the hinode mission. *Sol. Phys.* 243, 63–86. doi:10.1007/s11207-007-0182-1
- Harra, L. K., Hara, H., Doschek, G. A., Matthews, S., Warren, H., Culhane, J. L., et al. (2017). Measuring velocities in the early stage of an eruption: Using “overlappogram” data from hinode EIS. *ApJ* 842, 58. doi:10.3847/1538-4357/aa7411
- Harra, L. K., Williams, D. R., Wallace, A. J., Magara, T., Hara, H., Tsuneta, S., et al. (2009). Coronal nonthermal velocity following helicity injection before an X-class flare. *ApJL* 691, L99–L102. doi:10.1088/0004-637X/691/2/L99
- Hinode Review Team Al-Janabi, K., Antolin, P., Baker, D., Bellot Rubio, L. R., and Bradley, L. (2019). Achievements of Hinode in the first eleven years. *PASJ* 71, R1. doi:10.1093/pasj/psz084
- Inglis, A. R., Ireland, J., Shih, A. Y., and Christe, S. D. (2021). Evaluating pointing strategies for future solar flare missions. *Sol. Phys.* 296, 153. doi:10.1007/s11207-021-01896-0
- Jeffrey, N. L. S., Fletcher, L., Labrosse, N., and Simões, P. J. A. (2018). The development of lower-atmosphere turbulence early in a solar flare. *Sci. Adv.* 4, 2794. doi:10.1126/sciadv.aav2794
- Landi, E., Li, W., Brage, T., and Hutton, R. (2021). Hinode/EIS coronal magnetic field measurements at the onset of a C2 flare. *ApJ* 913, 1. doi:10.3847/1538-4357/abfd61
- Lemen, J. R., Title, A. M., Akin, D. J., Boerner, P. F., Chou, C., Drake, J. F., et al. (2012). The atmospheric imaging assembly (AIA) on the solar dynamics observatory (SDO). *Sol. Phys.* 275, 17–40. doi:10.1007/s11207-011-9776-8
- Lin, R. P., Dennis, B. R., Hurford, G. J., Smith, D. M., Zehnder, A., Harvey, P. R., et al. (2002). The reuven ramaty high-energy solar spectroscopic imager (rhessi). *Sol. Phys.* 210, 3–32. doi:10.1023/A:1022428818870
- Meegan, C., Lichti, G., Bhat, P. N., Bissaldi, E., Briggs, M. S., Connaughton, V., et al. (2009). THEFERMIGAMMA-RAY burst monitor. *ApJ* 702, 791–804. doi:10.1088/0004-637X/702/1/791
- Milligan, R. O. (2015). Extreme ultra-violet spectroscopy of the lower solar atmosphere during solar flares (invited review). *Sol. Phys.* 290, 3399–3423. doi:10.1007/s11207-015-0748-2
- Neupert, W. M. (1968). Comparison of solar X-ray line emission with microwave emission during flares. *ApJL* 153, L59. doi:10.1086/180220
- Pesnell, W. D., Thompson, B. J., and Chamberlin, P. C. (2012). The solar dynamics observatory (SDO). *Sol. Phys.* 275, 3–15. doi:10.1007/s11207-011-9841-3
- Thompson, W. T., and Brekke, P. (2000). EUV full-sun imaged spectral atlas using the SOHO coronal diagnostic spectrometer. *Sol. Phys.* 195, 45–74. doi:10.1023/A:1005203001242
- To, A. S. H., Long, D. M., Baker, D., Brooks, D. H., van Driel-Gesztelyi, L., Laming, J. M., et al. (2021). The evolution of plasma composition during a solar flare. *ApJ* 911, 86. doi:10.3847/1538-4357/abe85a
- Tolbert, K., and Schwartz, R. (2020). *Ospex: Object spectral executive*. Astrophysics Source Code Library. ascl:2007.018. Available at: <https://ascl.net>.
- Ugarte-Urra, I., Young, P. R., Brooks, D. H., Warren, H. P., De Pontieu, B., Bryans, P., et al. (2023). The case for solar full-disk spectral diagnostics: Chromosphere to corona. *Front. Astronomy Space Sci.* 9, 192. doi:10.3389/fspas.2022.1064192
- Warren, H. P., Brooks, D. H., Ugarte-Urra, I., Reep, J. W., Crump, N. A., and Doschek, G. A. (2018). Spectroscopic observations of current sheet formation and evolution. *ApJ* 854, 122. doi:10.3847/1538-4357/aaa9b8
- Watanabe, K., Masuda, S., and Segawa, T. (2012). Hinode flare catalogue. *Sol. Phys.* 279, 317–322. doi:10.1007/s11207-012-9983-y

Publisher's note

All claims expressed in this article are solely those of the authors and do not necessarily represent those of their affiliated organizations, or those of the publisher, the editors and the reviewers. Any product that may be evaluated in this article, or claim that may be made by its manufacturer, is not guaranteed or endorsed by the publisher.